https://doi.org/10.1016/j.apsusc.2022.155806

In-situ self-sacrificed fabrication of insulator-based $SrTiO_3/SrCO_3$ heterojunction interface for gaseous HCHO and NO photocatalytic degradation

Shuwen Han[a], Xinwei Li[a], Yan Tan[b,*], Yu Huang[c], Zhongbiao Wu[d], Meng Wang[a], Wingkei Ho[e], Shun-cheng Lee[a,*]

[a] *Department of Civil and Environmental Engineering, The Hong Kong Polytechnic University, Hong Kong SAR, China*

[b] *School of Environmental and Municipal Engineering, Qingdao University of Technology, Qingdao, China*

[c] *State Key Laboratory of Loess and Quaternary Geology, Institute of Earth Environment, Chinese Academy of Sciences, Xi'an, China*

[d] *Key Laboratory of Environment Remediation and Ecological Health, Ministry of Education, College of Environmental and Resource Sciences, Zhejiang University, Hangzhou, China*

[e] *Department of Science and Environmental Studies, The Education University of Hong Kong, Hong Kong SAR, China*

Corresponding Authors:

Shun-cheng Lee (shun-cheng.lee@polyu.edu.hk)

Yan Tan (tanyan@qut.edu.cn)

Abstract

In this work, novel heterostructured $SrTiO_3/SrCO_3$ (STO/SCO) interface was constructed via the one-pot g-C_3N_4(CN) self-sacrificing hydrothermal strategy. The as-developed STO/SCO photocatalyst shows the air cleaning potential in continuous-flow reactors with degradation rates of NO and HCHO at 44% and 40%, respectively. From XRD, FTIR, and XPS analysis, CN participates in the crystallise process as the source of CO_3^{2-} to form the STO/SCO interface viewed by TEM and HRTEM. Subsequent temperature-programmed desorption (TPD) analysis and density functional theory (DFT) calculation results revealed the enhanced chemisorption effects of O_2 on the catalyst surface. The existence of oxygen vacancies combined with the formation of heterojunction surface induces intermediate levels, which leads to the photocatalytic oxidation under simulated solar light. Charge difference distribution simulation coupled with electrochemistry and photoluminescence tests confirmed the internal-built electron fields at the heterojunction interface which would be beneficial for photocarriers separation. Based on the above-mentioned effects, enhanced reactive oxygen species (ROS) •OH and $\bullet O_2^-$ were detected under light irradiation by electron spin resonance (ESR). This work demonstrates the effectiveness of in-situ self-sacrificed strategy for construction of heterojunction interfaces and provides opportunities by utilising insulator-based materials for photocatalytic degradation of air pollutants.

Keywords: Insulator-based photocatalyst; Oxygen activation; $SrTiO_3/SrCO_3$ Heterojunction interface; NOx and HCHO removal

1. Introduction

Indoor air quality has attracted much attention and becomes a public concern globally, particularly after the outbreak of the respiratory virus SARS-CoV-2 (COVID-19) [1,2]. Nitrogen oxides (NO_x) and volatile organic compounds (VOCs) are major indoor air pollutants generated from fireplaces, kitchen activities, furniture materials, cigarettes and personal care products [3,4]. In general, NO_x and HCHO are the most common gaseous pollutants and have adverse health effects on human beings [5–7]. The indoor concentrations of NO_x and HCHO often exceed the standards set by World Health Organization, which are 150 $\mu g/m^3$ and 100 $\mu g/m^3$, respectively [8,9]. Therefore, a promising technology is expected to be developed to deal with the high concentrations of NO_x and HCHO.

Photocatalysis is an effective and environmentally friendly technology widely applied for air pollutants removal without consuming extra energy and little secondary pollution [10–14]. Traditionally, photocatalysts are semiconductors (e.g., TiO_2) [15,16] and some noble metals (plasmonic metals, e.g., Au and Ag) [17–19]. Earth-abundant insulators have great properties such as cheap price, stable chemistry and easy fabrication as compared with the abovementioned semiconductors and plasmonic metals [20,21]. However, insulators suffer application obstacles because of their wide band gaps which are difficult to be excited as compared to those semiconductors. Nevertheless, the wide band gaps of the insulator photocatalyst could offer excellent redox ability [22]. Recently, various strategies have been developed to modify the wide-gap insulators in resolving the bottleneck problem [17,23]. Thereinto, the combination of semiconductors and insulators for the construction of heterojunctions could promote the efficiency of light utilisation and the capacity of oxidation reactions at the same time [24,25]. The methods for the construction of heterojunction structures include co-

polycondensation, post-modification, ion exchange, hydrothermal hydrolysis, in-situ synthesis, template method, etc. [26–28]. The in-situ self-sacrificial method synthesizes the heterojunction structure by utilizing the template material as the sacrificial agent and then converting it into another counterpart. Due to its chemical transformation in the heterojunction formation process, there would be a well-combined interface with the two components possessing strong interactions [28,29]. Wang et al. [30] and Huang et al. [31] have reported the g-C_3N_4 self-sacrifice fabrication of $Bi_2O_2CO_3$/g-C_3N_4 and $Bi_xO_yI_z$/g-C_3N_4. By using the in-situ self-sacrifice strategy, Liu et al. [32] have synthesized the metal-organic frameworks and Hu et al. [33] have fabricated heterostructured β-Bi_2O_3/$Bi_2O_2CO_3$ microspheres successfully.

Typically, strontium titanate ($SrTiO_3$, STO) is a natural abundant semiconductor and a cubic perovskite with superior photocatalytic redox potential and provides higher efficiency in the photocatalytic process than TiO_2 [34]. Insulator strontium carbonate ($SrCO_3$, SCO) is developed as a catalyst or co-catalyst and displays superior photocatalytic activity for air pollutants removal [35,36]. Considering the unique features of STO and SCO, fabrication of $SrTiO_3$/$SrCO_3$ heterojunction has been verified to incorporate the merits of each component, and then to develop the application potential in air pollution control. [37,38]. In this study, we constructed an insulator-based STO/SCO heterojunction interface for the first time with a facile one-pot in-situ self-sacrificed strategy by utilizing g-C_3N_4 as the template and carbonate source. The as-prepared STO/SCO heterojunctions are verified the air cleaning ability by effectively photo-degrading the typical indoor air pollutants NO and HCHO at different concentration levels. Experimental analysis and theoretical calculation are combined to study the mechanism of photocatalytic air purification over STO/SCO heterojunction and provide a new strategy for the application of insulator-based photocatalysts.

2. Experimental

2.1 Construction of $SrTiO_3/SrCO_3$ heterojunction interface

g-C_3N_4 (CN) was synthesised through the pyrolysis method using an analytical grade urea. In a general process, a total of 10 g of urea and 30 mL of deionised water were placed in a crucible and stirred evenly. The sample is oven-dried at 60 °C, and then heated at 550 °C in a muffle furnace for 2 hours. Subsequently, the obtained light yellow powder CN sample was grounded and properly stored for future use.

$SrTiO_3/SrCO_3$ composites (STO/SCO for short) were synthesised through the hydroxide-mediated hydrothermal method. Normally, 0.30 mL of tetrabutyl titanate ($C_{16}H_{36}O_4Ti$, Aladdin Co., Ltd, Chemical Grade, China) was added to 25 mL of absolute ethyl alcohol (C_2H_5OH, Sinopharm Chemical Reagent Co., Ltd, Analytical Grade, China). A semi-transparent light-white solution was obtained by continuous mixing using a magnetic stirrer. 1 mmol of strontium nitrate ($Sr(NO_3)_2$, Sinopharm Chemical Reagent Co., Ltd, Analytical Grade, China) was added to the mixed liquid with persistent stirring. Then, a total of 10 mL of 0.4 $mol \cdot L^{-1}$ sodium hydroxide (NaOH, Sinopharm Chemical Reagent Co., Ltd, Analytical Grade, China) solution was mixed into the liquid with continuous stirring for 30 mins. Afterwards, 0.018 g of prepared CN powder sample was added with continuous stirring for another 60 mins. Then, the mixture was transferred and sealed into a 100 mL Teflon-lined autoclave to be heated at 160 °C for 24 h. After cooling down to room temperature, the $SrTiO_3/SrCO_3$ heterojunction (denoted as STO/SCO-1) was obtained after rinsing with absolute ethanol and water thrice. STO/SCO composites with different weight ratios (denoted as STO/SCO-2, STO/SCO-3) were fabricated by changing the added weight of CN (0.046 g and 0.092 g), respectively. The pure $SrTiO_3$ (STO) sample was also prepared by

following the same process without adding CN. The pure $SrCO_3$ (SCO) of analytical grade was purchased from Aladdin.

2.2 Characterisation methods and DFT calculation

The detailed methods for catalyst characterisations and DFT computational calculation are described in the Supporting Information (SI).

2.3 Photocatalytic activity test

The efficiencies of the photocatalytic removal of the as-prepared catalysts for HCHO and NO were evaluated using two well-designed continuous-flow reactors. The volumes of the reactors were 0.4 L (20 cm × 10 cm × 2 cm) for HCHO reaction and 4.5 L (30 cm × 15 cm × 10 cm) for NO reaction, respectively, and the details of the two reactors were described in previous studies [10,39]. A 300 W commercial Xe arc lamp (microsolar 300, Perfectlight, China) was vertically placed outside the reactor. 0.1 g of catalyst was added into 2 mL distilled water and then coated onto a glass dish with a diameter of 8 cm. After being treated at 60 °C, the coated dish was placed in the centre of the reactor to evaporate water and then cooled down to room temperature. The standard HCHO gas was supplied by a compressed gas cylinder with the HCHO concentration at 50 ppm (N_2 balance), whilst NO was acquired from another gas cylinder with the NO concentration at 49.6 ppm (N_2 balance) conforming to the standard of the National Institute of Standards and Technology (NIST). A zero-air initiator (Model 111, Thermo Environmental Instruments Inc., USA) generated an air stream that was separately mixed in a gas dilution calibrator (Model T700, Teledyne Technologies Inc., USA) with HCHO or NO. The preset concentrations of HCHO and NO were diluted to 1 ppm and 400 ppb with the controlled flow rate of 1 L min^{-1}, respectively. Once the equilibrium of adsorption-desorption was achieved, the lamp was then turned on to initiate the photocatalytic reaction. The concentration of HCHO

was measured by an online Photoacoustic IR multi-gas monitor (Model 1412, INNOVA Air Tech Instruments, Denmark). Chemiluminescence $NO/NO_2/NO_X$ analyser (Model T200, Teledyne Technologies Inc., USA) was used to continuously measure the NO concentration and the removal efficiency (η) of each typical pollutant (HCHO or NO) was calculated by Eq. (1):

$$\eta\ (\%) = (1- C_t/C_0) \times 100\ \% \quad (1)$$

where C_t is the outlet concentration of the typical pollutant at the reaction time of t, and C_0 represents the initial inlet concentration.

3. Results and discussion

3.1 In-situ self-sacrificed fabrication of $SrTiO_3/SrCO_3$ heterojunction

STO samples were synthesised by the hydroxide-mediated hydrothermal process and STO/SCO heterojunctions were prepared by adding different contents of carbonous precursor CN. The phase compositions of synthesised STO, STO/SCO-1,2,3, and SCO samples were characterised by X-ray diffraction (XRD). **Fig. 1(a)** shows the XRD pattern of STO that matches well with the standard $SrTiO_3$ (PDF#35-0734) and no other diffraction peak is detected, indicating the pristine $SrTiO_3$ structure of the STO sample. The diffraction peaks of $SrTiO_3$ are also detected in synthesised STO/SCO-1,2,3 heterojunction samples. Another group of distinct peaks at 25.2°, 25.8°, 29.6°, 31.3°, 34.5°, 35.1°, 36.2°, 36.5°, 41.3°, 44.1°, 45.6°, 47.7° and 49.9°, which could be indicated to the (111), (021), (002), (121), (102), (200), (112), (130), (220), (221), (041), (132) and (113) crystal planes of orthorhombic $SrCO_3$ (PDF#05-0418), are indexed respectively. The two crystal groups of STO and SCO in STO/SCO samples are independent phases without any position shift of diffraction peaks, suggesting that there was no lattice distortion occurred. With the increasing addition contents of CN, the XRD patterns of $SrCO_3$ become prominent in STO/SCO heterojunctions. Further XRD

phase quantitative analysis [40] results of STO/SCO-1,2,3 samples shown in Table S1 demonstrate that 71.5% contents of SCO are found in STO/SCO-3 sample based on XRD Rietveld refinement [41,42]. It was followed by STO/SCO-2 and STO/SCO-1 samples with 66.7% and 17.3% contents of SCO, respectively. The weight ratio of SCO is positively related to the additional contents of CN.

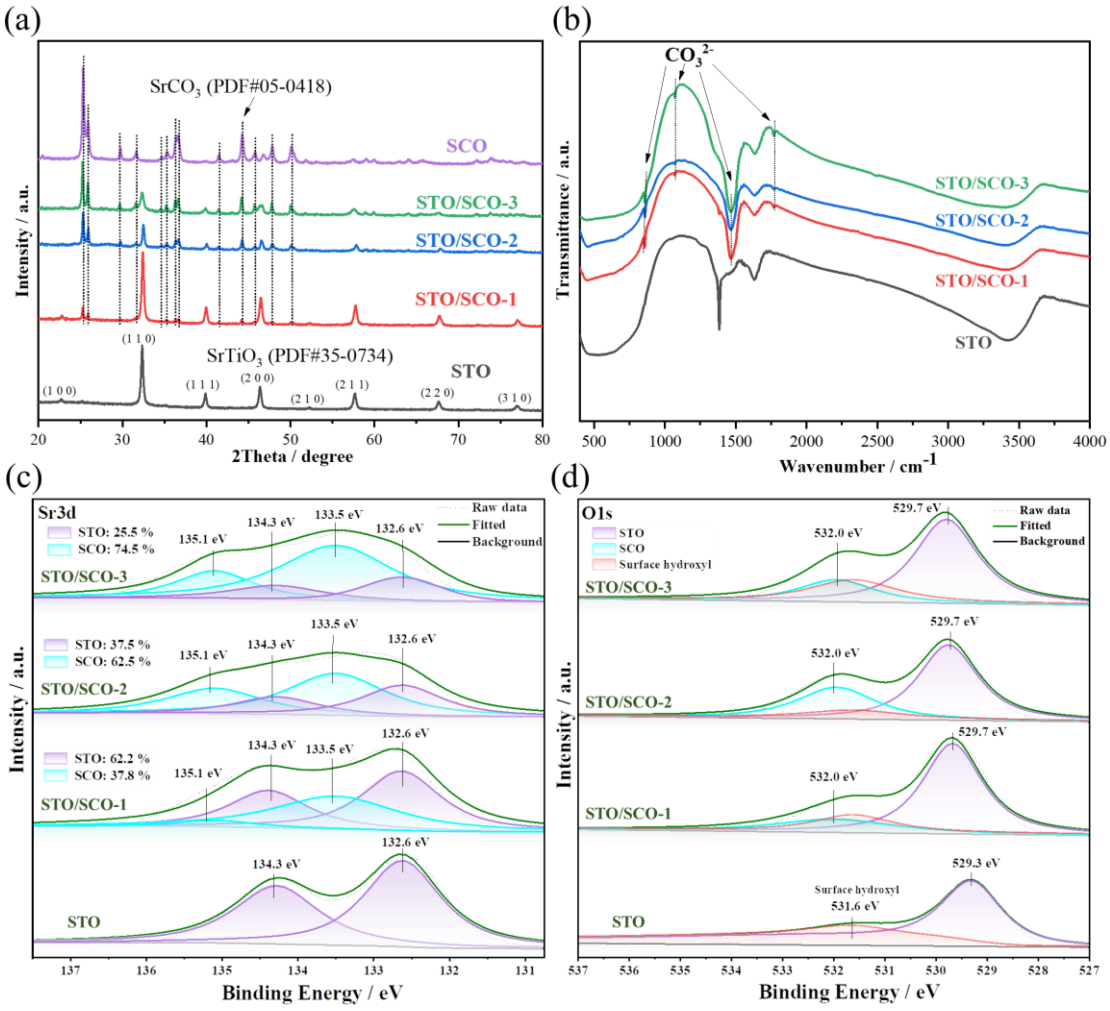

Fig. 1. (a) XRD patterns of SCO, STO/SCO-1,2,3 and STO; (b) FT-IR spectra of STO and STO/SCO-1,2,3; and XPS spectra of (c) Sr3d and (d) O1s for STO and STO/SCO-1,2,3

Fig. 1(b) shows the FT-IR spectra of the STO and STO/SCO-1,2,3. Four distinct absorption bands at 820 cm^{-1}, 1067 cm^{-1}, 1468 cm^{-1} and 1756 cm^{-1} in STO/SCO samples are identified as functional groups of CO_3^{2-} at out-of-plane bending mode, symmetric

stretching mode, corresponding anti-symmetric vibration and both out-of-plane bending mode and in-plane deformation, respectively [43]. Therefore, confirming the existence of CO_3^{2-} in STO/SCO components. In addition, no feature peak of CN [30] was found in STO/SCO samples, implying that CN was completely decomposed during the hydroxide-mediated hydrothermal process. The surface chemical states of as prepared samples were further investigated by the XPS profiles. **Fig. S1** displays the full-scan spectra of, Sr, Ti, O and C elements in STO and STO/SCO heterojunction samples as expected. For the Sr 3d spectra of pristine STO sample in **Fig. 1(c)**, the binding energy at 132.6 eV (Sr $3d_{5/2}$) and 134.3 eV (Sr $3d_{3/2}$) attribute to Sr^{2+} state of $SrTiO_3$ [44]. While Sr 3d XPS spectra of the STO/SCO-1,2,3 samples are fitted into four characteristic peaks with binding energy at the 132.6 eV (Sr $3d_{5/2}$) and 134.3 eV (Sr $3d_{3/2}$) attributed to $SrTiO_3$, and at the 133.5 eV (Sr $3d_{5/2}$) and 135.1 eV (Sr $3d_{3/2}$) referred to Sr^{2+} of $SrCO_3$ [44], respectively. Also, the Sr^{2+} ratio of SCO part in STO/SCO samples increases from 37.5 % in STO/SCO-1 to 62.5 % in STO/SCO-2, and then to 74.5 % in STO/SCO-3, which indicates the addition of CN promotes the formation of SCO in crystal growth. This constitution results are consistent with the previous XRD and FTIR analysis. The O 1s spectrum of STO shown in **Fig. 1(d)** is fitted into two peaks at around 529.7 eV, and 531.6 eV, which are ascribed to Sr-O-Ti in $SrTiO_3$ and surface hydroxyl species, respectively. The O 1s of STO/SCO samples are divided into three peaks at 532.0 eV, 531.6 eV and 529.7, which attribute to Sr-O-C in SCO, surface hydroxyl species, and Sr-O-Ti in $SrTiO_3$ respectively. There is a slight peak deviation observed in STO/SCO samples for oxygen bound to Sr and Ti, owing to the construction of heterojunction between $SrTiO_3$ and $SrCO_3$. Ti $2p_{1/2}$ and Ti $2p_{3/2}$ peaks indicating the exist of Ti^{4+} [45] are identified in **Fig. S2(a)**. The binding energy of Ti 2p for STO/SCO samples shift to higher energy direction compared with

STO sample due to the surface interaction between the STO and SCO counterparts of the heterojunction structure [46]. C 1s in **Fig. S2(b)** is fitted into two distinct peaks. The peak at 284.8 eV is attributed to the adventurous carbon compounds, whereas the peak at 289.4 eV corresponds to O-C=O of the carbonate in $SrCO_3$ [47]. The enhancement of O-C=O peaks confirms the gradual increase of SCO from STO/SCO-1 sample to STO/SCO-3 sample. All the above XPS results indicate the formation of STO/SCO heterojunction with strong chemical bonds interaction.

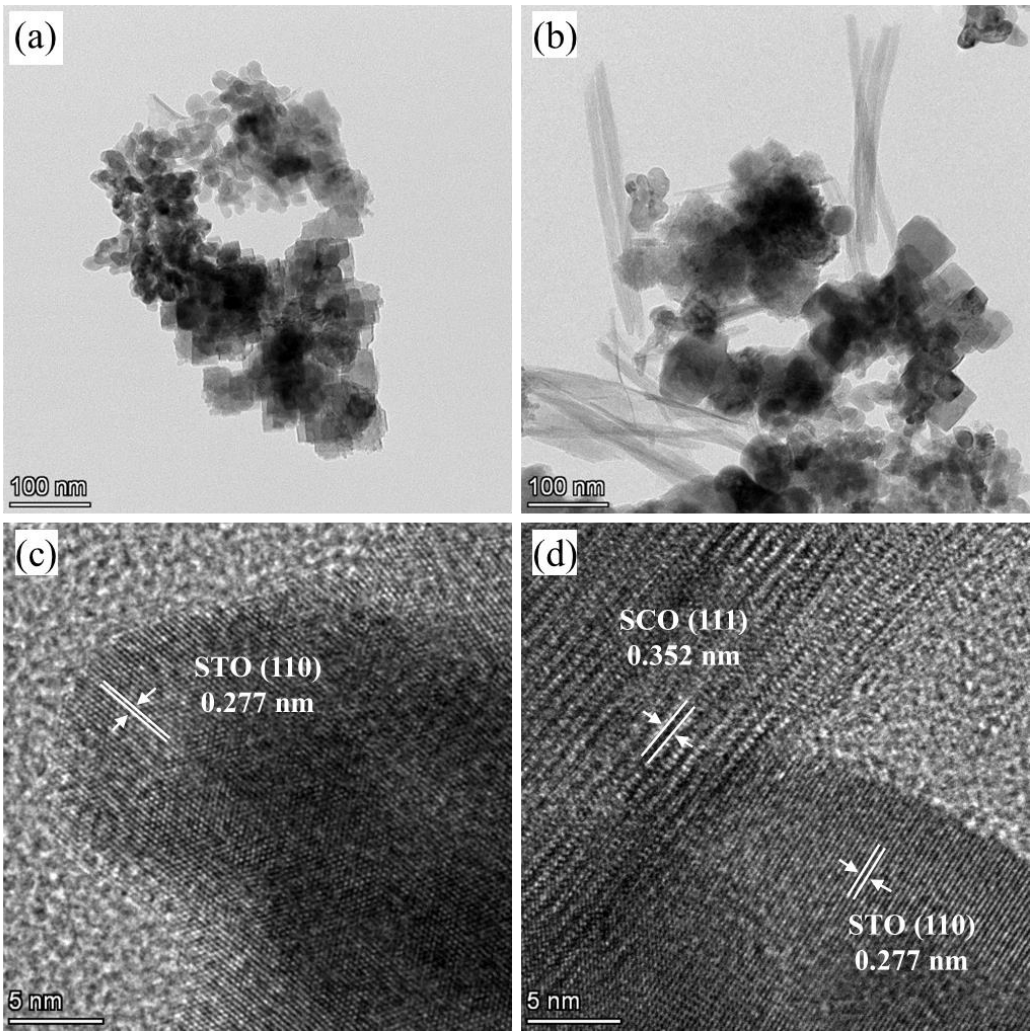

Fig. 2. TEM of the (a) STO and (b) STO/SCO-2 and HRTEM of the (c) STO and (d) STO/SCO-2

As visualised by the SEM image in **Fig. S3(a) and S3(b)**, typical STO sample is composed of various nanoparticle structure stacked together. While in STO/SCO

heterojunctions samples (**Fig. S3 (c-h)**), two types of characteristics morphologies are identified, namely nanoparticles and nanorods, which attribute to the formation of STO/SCO heterojunction structures. In catalytic reaction, the rough surface and crack structure amongst nanoparticles would be assumed to be beneficial for the adsorption process [48]. Related elements mappings in **Fig. S4** indicate that these elements are evenly distributed on STO/SCO-2 sample. **Table 1** shows the lists of the atomic ratios of Sr/Ti based on the EDS analysis, and the Sr/Ti ratio increases from 1/0.89 to 1/0.66 for STO/SCO-2 compared with the original STO. The decrease of the Ti element implies there are other compounds engaged to react with the precursor of Sr. The TEM and HRTEM images of both STO and STO/SCO-2 samples were obtained to view the detailed morphology and the interface of the as constructed STO/SCO heterojunction. The TEM image presented in **Fig 2(a)** further confirms the pileup of nanostructure of STO. Besides the similar nanostructure of STO, another kind of rods-like nanostructures are viewed in STO/SCO-2 sample, as pre-viewed in SEM image. The HRTEM image of STO sample in **Fig 2(c)** displays clear lattice spacing of 0.277 nm, which are well agreed with the (110) crystal plane of STO. For the corresponding HRTEM image of STO/SCO-2 sample in **Fig 2(d)**, lattice spacings viewed of 0.277 nm and 0.352 nm are referred to the (110) crystal plane of STO and (111) crystal plane of SCO, respectively. The HRTEM image of the STO/SCO-2 sample evidences the formation of heterojunction interface with intimate contact, which promotes the transmission and separation of photo-generated carriers. In addition, as listed in **Fig. S5(a)**, the specific surface areas detected by BET methods are found to increase with the gradually addition of CN. And as shown in **Fig. S5(b)**, no obvious change of the crystal size for different combinations can be observed by BJH pore size distribution. Based on the results of materials characterisation, the process of STO/SCO

heterojunction formation is deduced as follows. TiO_3^{2-} hydrolysed from the precursor of tetrabutyl titanate and Sr^{2+} that originated from $Sr(NO_3)_2$ will crystalise to STO during the hydrothermal process. Considering that CO_3^{2-} from hydrolysed CN participates in the reaction system, the precursor of Sr would also react with this C source in simultaneously generating SCO under alkaline condition and finally contributes to the construction of STO/SCO heterojunctions interface [49,50]. **Fig. 3** shows the schematic illustration of the synthesis processes of STO/SCO heterojunctions.

Table 1 Elemental analyses of the STO/SCO-2, STO and SCO compounds by EDS

Element	Atomic of STO/SCO-2 (%)	Atomic of STO (%)	Atomic of SCO (%)
Sr	20.79	15.18	25.05
Ti	13.65	17.08	0.00
O	65.56	67.74	74.95
Sr: Ti	1: 0.66	1: 0.89	-

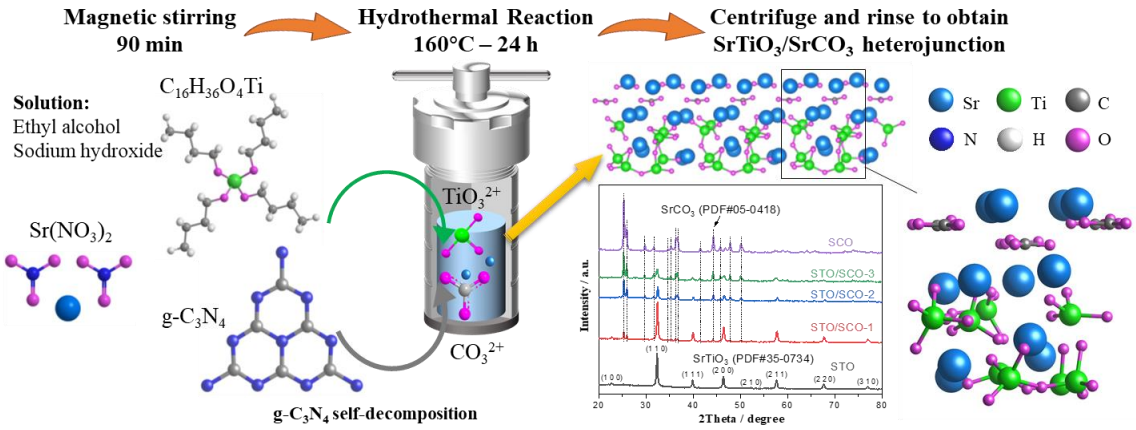

Fig. 3. Schematic illustration of the synthesis processes of STO/SCO heterojunctions

3.2 Photocatalytic degradation of HCHO and NO by $SrTiO_3/SrCO_3$ heterojunction

The photocatalytic air purification potentiality of the as-prepared STO and STO/SCO-X (X = 1,2,3) samples were evaluated in continuous reaction systems under simulated

solar light irradiation. HCHO and NO were chosen as the representative target air pollutants. **Fig. 4(a)** displays the time-varying concentrations of HCHO (C/C_0 %) with the as-prepared photocatalysts under light irritation. The HCHO concentrations sharply decline in the first 6 mins and become steady as the equilibration of the photocatalytic reaction. After irradiating for 30 mins, the removal efficiencies of HCHO by STO, STO/SCO-1. STO/SCO-2 and STO/SCO-3 samples are 7.1%, 32.2%, 40.3% and 20.5%, respectively, whilst there is rare degradation for pristine SCO under similar conditions. As for the photocatalytic degradation of NO shown in **Fig. 4(b)**, the STO/SCO heterojunctions all exhibit improved capacities compared with both pristine STO and SCO. The removal case of NO is similar to that of the HCHO, STO/SCO-2 sample presents the highest removal efficiency of NO at around 44%. Considering that SCO cannot be activated under visible light irritation because of its wide band gap [50], pristine SCO showed limited photocatalytic activity in both HCHO and NO degradation. The reaction rates of NO and HCHO photooxidation were calculated to quantitatively compare their capabilities. The early stage of photocatalytic degradation progress follows the mass-transfer-controlled pseudo-first-order rate reaction [51]. The reaction kinetics based on the Langmuir-Hinshelwood model is used and defined as Eq. (2) [52].

$$-\ln (C/C_0) = k\,t \quad (2)$$

where C and C_0 represent the concentrations after and before irradiation, respectively, meanwhile, k represents the apparent reaction rate constant and t is the irradiation time. The apparent reaction rate constant k is the slope of the plot of $-\ln (C/C_0)$ versus irradiation time t (min), which is demonstrated in **Fig. 4(c)** and **4(d)** for HCHO degradation and NO degradation, respectively. The apparent reaction rate constants of STO/SCO-2 are the largest for both HCHO (0.0646 min^{-1}) and NO (0.0782 min^{-1}) degradations amongst all the samples. Rates are 4.5 and 2.3 times higher for HCHO

and NO than those of pristine STO. Photodegradation experiments with different initial concentrations of both NO and HCHO were conducted to thoroughly study their photocatalytic effects. As shown in **Fig. S6**, The SCO/STO-2 sample exhibits almost the same reaction rates and degradation efficiencies for both NO and HCHO. Thus, the removal effectiveness can be confirmed for both high and low pollution situations. The above results indicate the STO/SCO-2 heterojunction is most effective in removing both NO and HCHO amongst all samples. The photocatalytic stability and reusability of STO/SCO-2 for degradation of both HCHO and NO were evaluated by repeated cyclic experiments to evaluate the potential applications for air purification. After five cycled runs, the removal efficiency of HCHO keeps the initial value of nearly 40% (**Fig. 3(e))**. Likewise, the efficiency for NO degradation also remains over 40% and consistent with almost the same level in all five tests. These results verify its outstanding reproducibility and stability for the purification of the two typical air contaminants in practice.

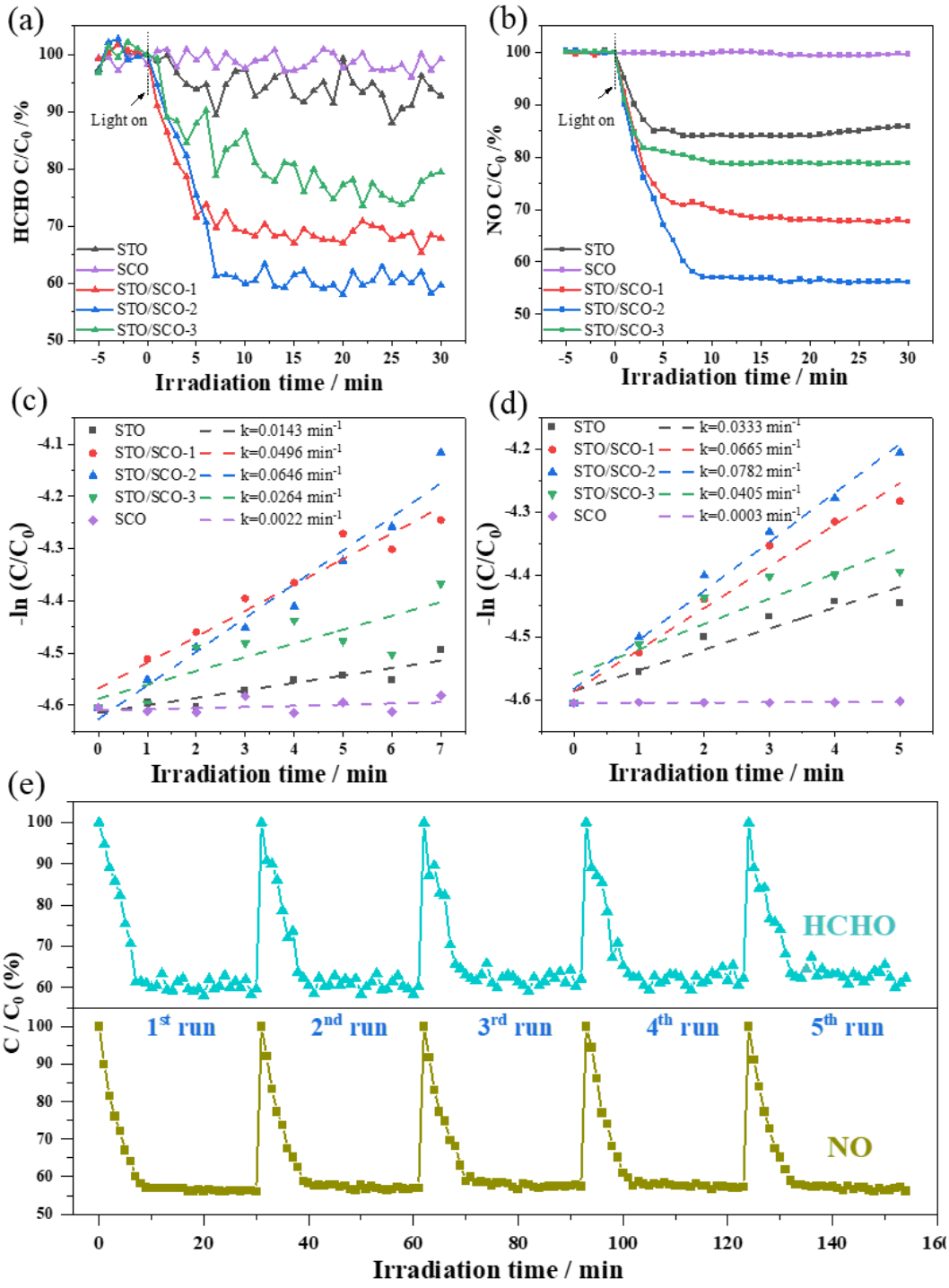

Fig. 4. Photocatalytic activities of STO, SCO and STO/SCO-1,2,3 for (a) HCHO and (b) NO removal; reaction rate constant k of STO, SCO and STO/SCO-1,2,3 for (c) HCHO and (d) NO removal; and (e) cycling runs for the HCHO and NO photocatalytic removal over STO/SCO-2.

3.3 The O_2 activation, and adsorption behaviour of HCHO and NO

The O_2 activation is generally considered the key step in photocatalytic reaction in environmental remediation application [53]. In this case, O_2 activation adsorption models are revealed by DFT calculation on the surfaces of STO, SCO and STO/SCO heterojunction (**Fig. 5**). **Table 2** shows the summary of the main calculation results. The bond length of O-O observed at the surface of STO is 1.32 Å whilst the O-O bond on STO/SCO surface is stretched to 1.45 Å. The adsorption energies of the O_2 molecule (E_{ads}) on the three composites are in the order of STO/SCO (-4.91 eV) < SCO (-4.72 eV) < STO (-1.14 eV) despite the O_2 bond length on SCO is 1.50 Å. The STO/SCO is determined to be more effective for O_2 activation than STO with lower E_{ads} and elongated O-O bond which is the same as SCO.

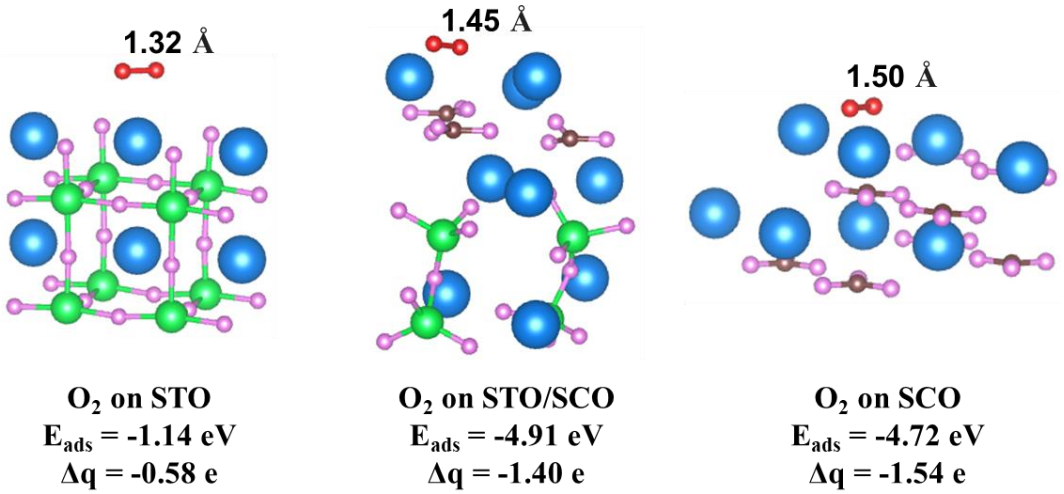

Fig. 5. Optimised O_2 adsorption on STO, STO/SCO and SCO configuration.

The HCHO and NO adsorption behaviours on the catalyst surface are before their photocatalytic reactions, and the adsorption/desorption performances are extremely necessary to determine the photocatalytic reaction [54]. The temperature-programmed desorption (TPD) was employed to investigate the behaviour between HCHO and the as-synthesised photocatalysts. The adsorption process of HCHO on the catalyst was conducted at room temperature till equilibrium. As illustrated in **Fig. 6**, there is one

distinguished desorption peak for the STO/SCO-2 sample at the temperature of nearly 500 °C representing the cleavage of the C = O bond of the intermediates formate (HCOOH) from HCHO oxidation [55]. However, no clear peak can be identified in the STO catalyst, indicating the HCHO chemisorption process does not occur on the surface of STO.

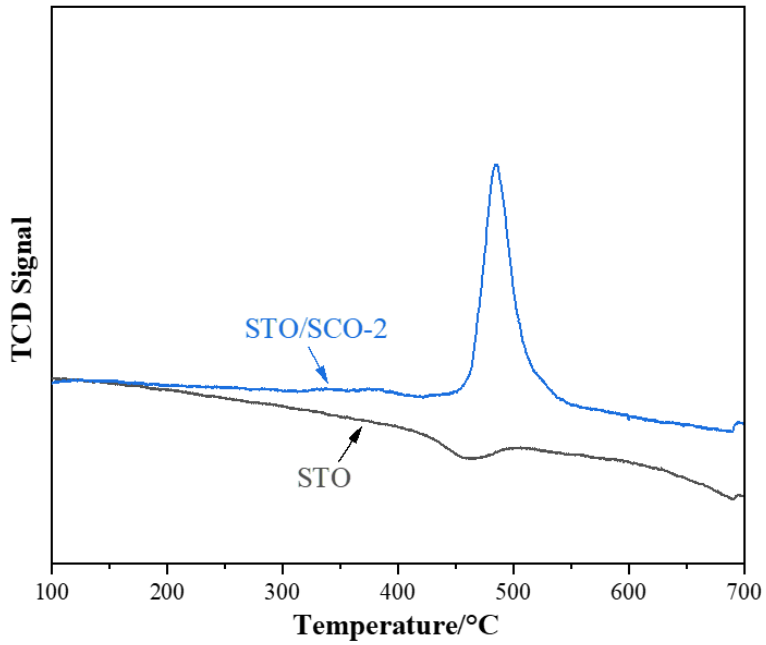

Fig. 6. HCHO-TPD profiles of STO/SCO-2 and STO.

The adsorption configurations of HCHO (**Fig. 7 (a)**) and NO (**Fig. 7 (b)**) onto STO, SCO and STO/SCO were calculated through DFT, respectively, to further explore the interactions between the gas pollutant molecules and the catalysts. The adsorption energy E_{ads} of HCHO molecules on STO/SCO structure is calculated to be -1.92 eV, which is 4 times and 1.2 times lower than those on the pristine STO and SCO structure, respectively whilst the charge depletion (Δq) also increases from -0.17 e on STO to -0.94 e on STO/SCO by the Bader method [56]. The heterojunction structure of STO/SCO in line with HCHO-TPD would facilitate the HCHO chemisorption process. In the NO adsorption process, the E_{ads} and Δq of NO on STO/SCO structure are found to be -2.80 eV and -1.11 e, which are about 6.7 times lower than STO structure of -0.42

eV and 4.6 times lower of Δq of -0.24 e, respectively. In addition, the N-O bond length of adsorbed NO varies from 1.19 Å on STO to 1.29 Å on STO/SCO, respectively. This indicates that the NO adsorption process would also be influenced by constructing the heterojunction. Both experimental and DFT calculation results validate the STO/SCO heterojunction surface promotes both the O_2 activation and air pollutants adsorption process.

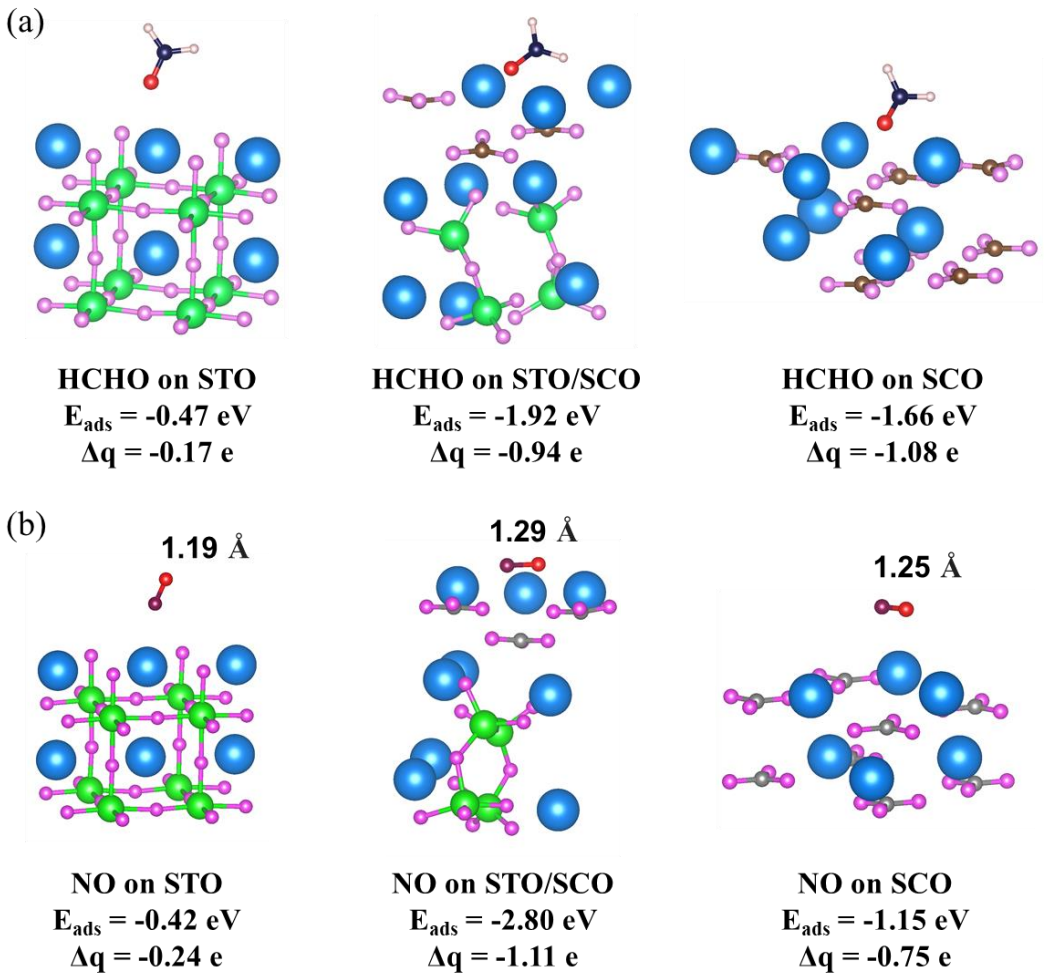

Fig. 7. Optimised (a) HCHO adsorption; (b) NO adsorption on STO, STO/SCO and SCO configuration. Δq and E_{ads} represent the carried electrons and adsorption energy.

3.4 Band structure and Photo-charge transfer

The surface work functions of SCO and STO were obtained as 5.41 eV and 4.81 eV by theoretical calculation, respectively, to further understand the effects of STO/SCO

heterojunction as shown in **Figs. 8(a)** and **8(b)**. The unequal work functions of SCO and STO spontaneously induce the charge migration at the interface by Colombian force, thereby effectively inhibiting the recombination of photoexcited carriers [35,57]. When the STO/SCO heterojunction is formed, electrons will transfer from the STO to the SCO's side with a lower work function to achieve the equilibrium of the Fermi levels (**Fig. S7**). Consequently, the charge distribution of the optimised STO/SCO geometry was also obtained as shown in **Fig. 8(c)**. The value of total charges (Δq) calculated through the Bader method for SCO is -1.74 e, indicating that SCO will receive 1.74 e electrons from STO, further confirming the direction of electron transfer is from STO to SCO (**Fig. 8(c))**. The main agent of reactant adsorption is the electron transportation at the STO/SCO interface and tends to reinforce the separation rate between photogenerated holes and electrons. The transient photocurrent was tested to probe the migration of photocatalytic electrons. The photocurrent signal excited over the STO/SCO-2 heterojunction (7×10^{-7} A·cm^{-2}) is the highest among the three prepared STO/SCO samples and is about 4 times higher than that of the STO sample as demonstrated in **Fig. 8(d)**. The SCO sample exhibits nearly no photocurrent because of its dielectric properties. Moreover, the photoluminescence (PL) spectra were tested to investigate the transmission and recombination rate of the photogenerated carriers. The excitation wavelength was set as 310 nm. As observed in **Fig. S8**, all the STO/SCO samples exhibit much lower PL peaks compared with pristine STO sample, which is caused by the formation of heterojunction interface that inhibiting the recombination of the photo-generated carriers. These results are consistent with our hypothesis of STO/SCO heterojunction.

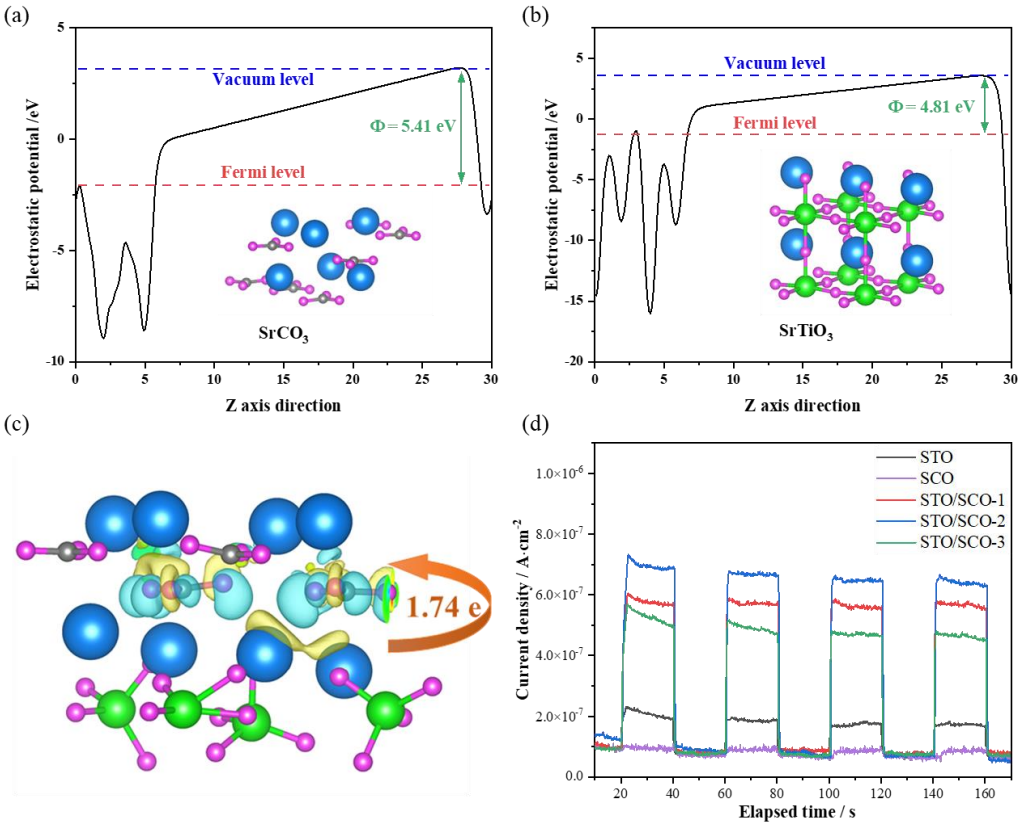

Fig. 8. The work functions of (a) $SrCO_3$ (001) surface; (b) $SrTiO_3$ (001) surface; (c) Charge difference distribution of the STO/SCO interfacial structure (blue and yellow represents charge accumulation and charge depletion, respectively); and (d) Transient photocurrent responses.

3.5 Understanding the mechanism of the photocatalytic air purification process

Measurements of ESR on STO, SCO and STO/SCO samples were performed under both simulated solar light irradiation and dark conditions by identifying the intensity of DMPO signals to ascertain the generation of ROS that are key elements in the photocatalytic purification process. **Fig. 9(a)** demonstrated the characteristic signals of DMPO-•O_2^- which can be recognised over STO/SCO-2 and STO samples after being simultaneously irradiated, and the signals of STO/SCO-2 is much stronger than those of STO. **Fig 9(b)** shows the characteristic peaks of DPMO-•OH for STO/SCO-2 and STO samples which exhibit the same patterns as •O_2^-. The STO/SCO-2 heterojunction enhances the generation of both •OH and •O_2^-, however, both the DMPO-•O_2^- and

DMPO-•OH are not detected for SCO because the insulator materials cannot respond to simulated solar light.

As for the band structure, the STO sample has a band gap energy of 3.22 eV with its absorption edge at 380 nm, whilst the absorption edge for the typical insulator of the SCO sample is at 285 nm with a band gap of 4.34 eV. The valence band (VB) and conduction band (CB) of STO and SCO are calculated to further seek insights by the following Eq. (3) and Eq. (4) [58]:

$$E_{VB} = X - E^e + 0.5\ E_g \quad (3)$$

$$E_{CB} = E_{VB} - E_g \quad (4)$$

where E_{VB}, E_{CB} and E_g are the VB, CB and the band gap of the compound, respectively. Meanwhile, X represents the electronegativity of the compound, which can be calculated from the electronegativity of each constituent atom, and E^e is the energy of free electrons on a hydrogen scale (~4.5 eV). For the STO, the electronegativity X and band gap E_g are obtained to be 4.95 eV and 3.22 eV, respectively. The E_{VB} and E_{CB} are further calculated to be 2.06 eV and -1.16 eV. Meanwhile, the electronegativity X and band gap E_g for SCO are determined to be 5.57 eV and 4.34 eV, respectively. The E_{VB} and E_{CB} for constituent SCO are 3.24 eV and -1.1 eV, respectively, as shown in **Fig. S9**. In addition, the solid ESR spectrum was used to determine the oxygen vacancy (OV) defects of STO/SCO-2 and STO. Two distinct symmetrical ESR signal peaks can be identified for the STO/SCO-2 sample at g = 2.002, whilst the STO sample shows no significant peak as demonstrated in **Fig. S10**. Restricted to band structure, pristine insulator SCO cannot be excited by simulated solar light because of its wide band gap, whilst the pristine STO is excited to produce limited photocatalytic charges. The existence of oxygen vacancies induces intermediate levels which render the opportunity to be excited by solar energy [59].

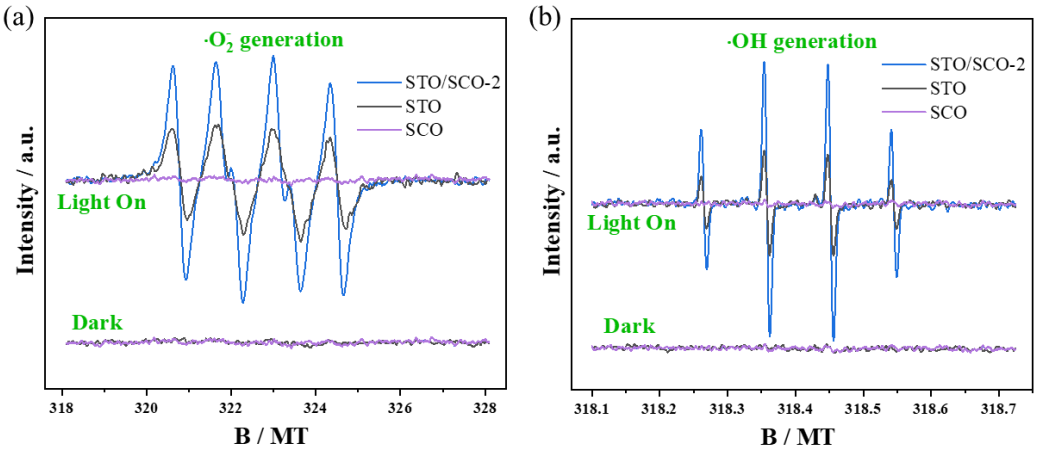

Fig. 9. DMPO spin-trapping ESR spectra of STO, STO/SCO and SCO samples in methanol dispersion for (a) DMPO-•O_2^-; in aqueous dispersion for (b) DPMO-•OH.

According to the results from the experimental analysis and theoretical calculation, the corresponding mechanism of photocatalytic air purification over STO/SCO heterojunction could be proposed in the following five processes demonstrated in **Fig. 10**. With the building of STO/SCO insulator heterojunction, electrons would be inclined to transfer from the STO to the SCO side at the interface in absence of light irradiation. This is because of the different potentials between the two parts that causes uneven distribution of charges, thereby promoting the construction of an internal electric field (process ①). The OVs were simultaneously generated during the formation of heterojunction rendering the possibility of direct transition from VB to intermediate level over SCO part to take large utilisation of solar light (process ②) and subsequently allows the photoexcited electrons transfer from intermediate level to the CB of SCO (process ③). Thus, the insulator-based STO/SCO heterojunction exhibits photocatalytic activities under simulated solar light irradiation. There will also be certain photoexcited electrons migrating from VB to CB as its weak light utilisation of STO (process ④). The existence of an internal electric field from process ① was beneficial in separating the photoexcited electron-hole pairs (process ⑤). The

accumulated holes at the VB of SCO will react with surface H_2O and hydroxy to generate •OH. In addition, the electrons gathered at the CB of SCO and STO react with O_2 to produce $•O_2^-$. Consequently, the robust ROS generation of both •OH and $•O_2^-$ would react with pre-adsorbed air pollutants NO or HCHO to achieve the target of air purification.

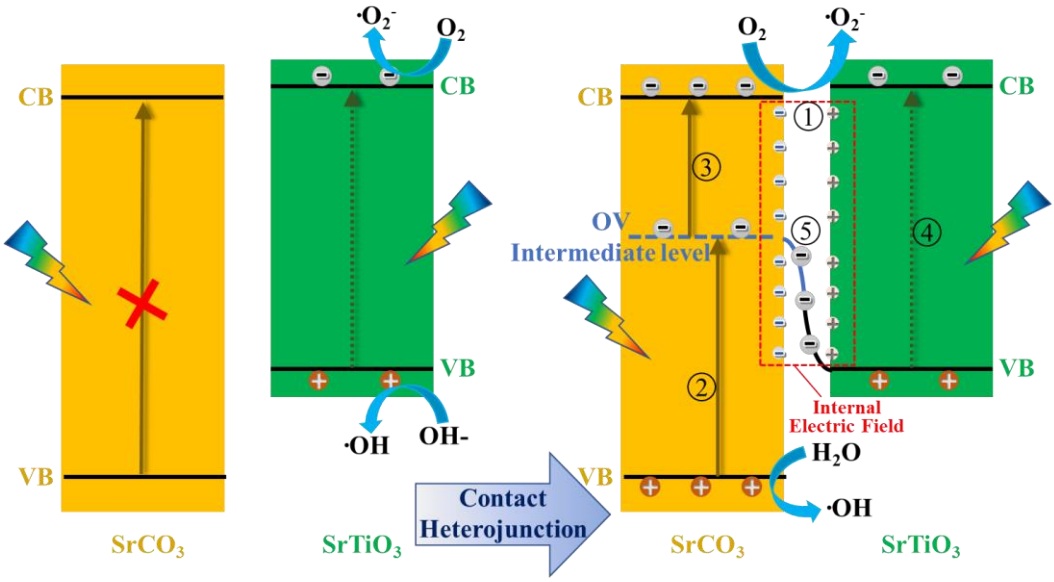

Fig. 10 Proposed photocatalytic mechanism to enhance photocatalytic activity over STO/SCO heterojunctions.

Table 2 Summary of bond length (N-O for NO and O-O for O_2), E_{ads} and Δq of adsorption on STO, SCO and STO/SCO, respectively.

Sample	HCHO		NO			O_2		
	E_{ads} (eV)	Δq (e)	N-O Length (Å)	E_{ads} (eV)	Δq (e)	O-O Length (Å)	E_{ads} (eV)	Δq (e)
STO	-0.47	-0.17	1.19	-0.42	-0.24	1.32	-1.14	-0.58
SCO	-1.66	-1.08	1.25	-1.15	-0.75	1.50	-4.72	-1.54
STO/SCO	-1.92	-0.94	1.29	-2.80	-1.11	1.45	-4.91	-1.40

4. Conclusion

Insulator-based STO/SCO nano-heterojunctions constructed by using the CN self-sacrificing hydrothermal synthesis method have been applied for the first time to purify the representative indoor air pollutants of NO and HCHO. The ideal photocatalytic activities (44% and 40%) and reaction rates (0.0782 min^{-1} and 0.0646 min^{-1}) towards both NO and HCHO can be achieved by optimising the ratio of counterparts of STO/SCO heterojunctions. A certain level of oxygen vacancies and the internal electric field were formed at the interface of the insulator-based STO/SCO heterojunction, which maximized the utilisation of solar energy to excite photocarriers and enhanced the transfer efficiency on the surface. Molecular O_2 is validated to be beneficially activated at the STO/SCO heterojunction surface with reduced adsorption energy from -1.14 eV to -4.91 eV, and enlarged O_2 bond from 1.32 Å to 1.45 Å based on the DFT calculation. The abundant ROS was generated with the combined effects of efficient photocarriers and stimulative O_2 activation for the photo-degradation of NO and HCHO. This study provides a feasible strategy for the design and fabrication of insulator-based photocatalysts applied for indoor air pollutants purification.

Acknowledgments

This work was supported by The Environment and Conservation Fund of Hong Kong Government (Project No. ECF 63/2019), The Research Grants Council of Hong Kong Government (Project No. T24/504/17 and T31-603/21-N)

Reference

[1] S.C. Lee, W.-M. Li, C.-H. Ao, Investigation of indoor air quality at residential homes in Hong Kong—case study, Atmos. Environ. 36 (2002) 225–237. https://doi.org/10.1016/S1352-2310(01)00435-6.

[2] Y. Liu, Z. Ning, Y. Chen, M. Guo, Y. Le Liu, N.K. Gali, L. Sun, Y. Sen Duan, J. Cai, D. Westerdahl, X.J. Liu, K. Xu, K.-F. Ho, H.D. Kan, Q.Y. Fu, K. Lan,

Aerodynamic analysis of SARS-CoV-2 in two Wuhan hospitals, Nature. 582 (2020) 557–560. https://doi.org/10.1038/s41586-020-2271-3.
[3] Y. Huang, W.K. Ho, S.C. Lee, L.Z. Zhang, G.S. Li, J.C. Yu, Effect of Carbon Doping on the Mesoporous Structure of Nanocrystalline Titanium Dioxide and Its Solar-Light-Driven Photocatalytic Degradation of NOx, Langmuir. 24 (2008) 3510–3516. https://doi.org/10.1021/la703333z.
[4] Y. Tan, S.W. Han, Y. Chen, Z.Z. Zhang, H.W. Li, W.Q. Li, Q. Yuan, X.W. Li, T. Wang, S.C. Lee, Characteristics and source apportionment of volatile organic compounds (VOCs) at a coastal site in Hong Kong, Sci. Total Environ. 777 (2021) 146241. https://doi.org/10.1016/j.scitotenv.2021.146241.
[5] D.Y.C. Leung, Outdoor-indoor air pollution in urban environment: challenges and opportunity, Front. Environ. Sci. 2 (2015) 69. https://doi.org/10.3389/fenvs.2014.00069.
[6] L.H. Nie, J.G. Yu, X.Y. Li, B. Cheng, G. Liu, M. Jaroniec, Enhanced Performance of NaOH-Modified Pt/TiO2 toward Room Temperature Selective Oxidation of Formaldehyde, Environ. Sci. Technol. 47 (2013) 2777–2783. https://doi.org/10.1021/es3045949.
[7] Y. Tan, S. Han, Y. Chen, Z. Wu, S. cheng Lee, Long-term variation and evaluation of air quality across Hong Kong, J. Environ. Sci. (China). 127 (2023) 284–294. https://doi.org/10.1016/j.jes.2022.05.009.
[8] HKEPD, IAQ Certification Scheme, 2022 (2019). https://www.iaq.gov.hk/en/iaq-certification-scheme-background/ (accessed June 7, 2022).
[9] WHO, WHO guidelines for indoor air quality: selected pollutants, World Health Organization. Regional Office for Europe, 2010. https://apps.who.int/iris/handle/10665/260127.
[10] X.W. Li, H.W. Li, Y. Huang, J.J. Cao, T.T. Huang, R. Li, Q. Zhang, S.C. Lee, W.K. Ho, Exploring the photocatalytic conversion mechanism of gaseous formaldehyde degradation on TiO2–x-OV surface, J. Hazard. Mater. 424 (2022) 127217. https://doi.org/10.1016/j.jhazmat.2021.127217.
[11] T.S. Natarajan, K.R. Thampi, R.J. Tayade, Visible light driven redox-mediator-free dual semiconductor photocatalytic systems for pollutant degradation and the ambiguity in applying Z-scheme concept, Appl. Catal. B Environ. 227 (2018) 296–311. https://doi.org/10.1016/j.apcatb.2018.01.015.
[12] J. Guo, C. Lin, C. Jiang, P. Zhang, Review on noble metal-based catalysts for formaldehyde oxidation at room temperature, Appl. Surf. Sci. 475 (2019) 237–255. https://doi.org/10.1016/J.APSUSC.2018.12.238.
[13] Y. Xie, S. Yu, Y. Zhong, Q. Zhang, Y. Zhou, SnO 2 /graphene quantum dots composited photocatalyst for efficient nitric oxide oxidation under visible light, Appl. Surf. Sci. 448 (2018) 655–661. https://doi.org/10.1016/j.apsusc.2018.04.145.
[14] X. Li, W. Zhang, J. Li, G. Jiang, Y. Zhou, S. Lee, F. Dong, Transformation pathway and toxic intermediates inhibition of photocatalytic NO removal on designed Bi metal@defective Bi2O2SiO3, Appl. Catal. B Environ. 241 (2019) 187–195. https://doi.org/10.1016/j.apcatb.2018.09.032.
[15] A. Nikokavoura, C. Trapalis, Graphene and g-C3N4 based photocatalysts for NOx removal: A review, Appl. Surf. Sci. 430 (2018) 18–52. https://doi.org/10.1016/j.apsusc.2017.08.192.
[16] Y. Huang, P.G. Wang, Z.Y. Wang, Y.F. Rao, J.J. Cao, S.Y. Pu, W.K. Ho, S.C. Lee, Protonated g-C3N4/Ti3+ self-doped TiO2 nanocomposite films: Room-

temperature preparation, hydrophilicity, and application for photocatalytic NOx removal, Appl. Catal. B Environ. 240 (2019) 122–131. https://doi.org/10.1016/j.apcatb.2018.08.078.

[17] A. Ziashahabi, M. Prato, Z. Dang, R. Poursalehi, N. Naseri, The effect of silver oxidation on the photocatalytic activity of Ag/ZnO hybrid plasmonic/metal-oxide nanostructures under visible light and in the dark, Sci. Rep. 9 (2019) 1–12. https://doi.org/10.1038/s41598-019-48075-7.

[18] G.Y. Yu, J. Qian, P. Zhang, B. Zhang, W.X. Zhang, W.F. Yan, G. Liu, Collective excitation of plasmon-coupled Au-nanochain boosts photocatalytic hydrogen evolution of semiconductor, Nat. Commun. 10 (2019) 1–8. https://doi.org/10.1038/s41467-019-12853-8.

[19] L. Lv, Y. Shen, J. Liu, X. Gao, M. Zhou, Y. Zhang, X. Meng, X. Yang, D. Gong, Y. Zheng, Z. Zhou, MX (M = Au, Ag; X = S, Se, Te) monolayers: Promising photocatalysts for oxygen evolution reaction with excellent light capture capability, Appl. Surf. Sci. 600 (2022) 154055. https://doi.org/10.1016/J.APSUSC.2022.154055.

[20] S. Schiavoni, F. D′Alessandro, F. Bianchi, F. Asdrubali, Insulation materials for the building sector: A review and comparative analysis, Renew. Sustain. Energy Rev. 62 (2016) 988–1011. https://doi.org/10.1016/j.rser.2016.05.045.

[21] F. Dong, T. Xiong, Y.J. Sun, L.L. Lu, Y.X. Zhang, H.J. Zhang, H.W. Huang, Y. Zhou, Z.B. Wu, Exploring the photocatalysis mechanism on insulators, Appl. Catal. B Environ. 219 (2017) 450–458. https://doi.org/10.1016/j.apcatb.2017.07.082.

[22] R.G. Li, X.L. Wang, S.Q. Jin, X. Zhou, Z.C. Feng, Z. Li, J.Y. Shi, Q. Zhang, C. Li, Photo-induced H2 production from a CH3OH-H2O solution at insulator surface, Sci. Rep. 5 (2015) 1–9. https://doi.org/10.1038/srep13475.

[23] Parul, K. Kaur, R. Badru, P.P. Singh, S. Kaushal, Photodegradation of organic pollutants using heterojunctions: A review, J. Environ. Chem. Eng. 8 (2020) 103666. https://doi.org/10.1016/j.jece.2020.103666.

[24] J. Xue, J.X. Liu, Y.M. Liu, H.L. Li, Y. Wang, D. Sun, W. Wang, L.J. Huang, J.G. Tang, Recent advances in synthetic methods and applications of Ag2S-based heterostructure photocatalysts, J. Mater. Chem. C. Mater. Opt. Electron. Devices. 7 (2019) 3943–3988. https://doi.org/10.1039/c9tc00008a.

[25] X. Dong, W.D. Zhang, Y.J. Sun, J.Y. Li, W.L. Cen, Z.H. Cui, H.W. Huang, F. Dong, Visible-light-induced charge transfer pathway and photocatalysis mechanism on Bi semimetal@defective BiOBr hierarchical microspheres, J. Catal. 357 (2018) 41–50. https://doi.org/10.1016/j.jcat.2017.10.004.

[26] Y. Liu, Z. Wang, W. Wang, X. An, S. Mi, J. Tang, W. Huang, Sandwich SrTiO3/TiO2/H-Titanate nanofiber composite photocatalysts for efficient photocatalytic hydrogen evolution, Appl. Surf. Sci. 315 (2014) 314–322. https://doi.org/10.1016/j.apsusc.2014.07.143.

[27] M. Zhang, Y. Duan, H. Jia, F. Wang, L. Wang, Z. Su, C. Wang, Defective graphitic carbon nitride synthesized by controllable co-polymerization with enhanced visible light photocatalytic hydrogen evolution, Catal. Sci. Technol. 7 (2017) 452–458. https://doi.org/10.1039/C6CY02318E.

[28] G. Wu, L. Yu, Y. Liu, J. Zhao, Z. Han, G. Geng, One step synthesis of N vacancy-doped g-C3N4/Ag2CO3 heterojunction catalyst with outstanding “two-path” photocatalytic N2 fixation ability via in-situ self-sacrificial method, Appl. Surf. Sci. 481 (2019) 649–660. https://doi.org/10.1016/j.apsusc.2019.03.112.

[29] Z.Y. Wang, Y. Huang, L. Chen, M.J. Chen, J.J. Cao, W.K. Ho, S.C. Lee, In situ g-C3N4 self-sacrificial synthesis of a g-C3N4/LaCO3OH heterostructure with strong interfacial charge transfer and separation for photocatalytic NO removal, J. Mater. Chem. A. 6 (2018) 972–981. https://doi.org/10.1039/C7TA09132J.

[30] Z.Y. Wang, Y. Huang, W.K. Ho, J.J. Cao, Z.X. Shen, S.C. Lee, Fabrication of Bi2O2CO3/g-C3N4 heterojunctions for efficiently photocatalytic NO in air removal: In-situ self-sacrificial synthesis, characterizations and mechanistic study, Appl. Catal. B Environ. 199 (2016) 123–133. https://doi.org/https://doi.org/10.1016/j.apcatb.2016.06.027.

[31] H. Huang, C. Liu, H. Ou, T. Ma, Y. Zhang, Self-sacrifice transformation for fabrication of type-I and type-II heterojunctions in hierarchical BixOyIz/g-C3N4 for efficient visible-light photocatalysis, Appl. Surf. Sci. 470 (2019) 1101–1110. https://doi.org/10.1016/j.apsusc.2018.11.193.

[32] T. Liu, P. Li, N. Yao, T. Kong, G. Cheng, S. Chen, W. Luo, Self-Sacrificial Template-Directed Vapor-Phase Growth of MOF Assemblies and Surface Vulcanization for Efficient Water Splitting, Adv. Mater. 31 (2019) 1806672. https://doi.org/10.1002/adma.201806672.

[33] R. Hu, X. Xiao, S. Tu, X. Zuo, J. Nan, Synthesis of flower-like heterostructured β-Bi2O3/Bi2O2CO3 microspheres using Bi2O2CO3 self-sacrifice precursor and its visible-light-induced photocatalytic degradation of o-phenylphenol, Appl. Catal. B Environ. 163 (2015) 510–519. https://doi.org/10.1016/j.apcatb.2014.08.025.

[34] W. Zhang, Y. Yu, Z.G. Yi, Controllable synthesis of SrCO.sub.3 with different morphologies and their co-catalytic activities for photocatalytic oxidation of hydrocarbon gases over TiO.sub.2, J. Mater. Sci. 52 (2017) 5106. https://doi.org/10.1007/s10853-017-0748-8.

[35] M. Kobayashi, Y. Suzuki, T. Goto, S.H. Cho, T. Sekino, Y. Asakura, S. Yin, Low-temperature hydrothermal synthesis and characterization of SrTiO3 photocatalysts for NOx degradation, J. Ceram. Soc. Japan. 126 (2018) 135–138. https://doi.org/10.2109/jcersj2.17195.

[36] S. Hodjati, K. Vaezzadeh, C. Petit, V. Pitchon, A. Kiennemann, Absorption/desorption of NOx process on perovskites: performances to remove NOx from a lean exhaust gas, Appl. Catal. B. 26 (2000) 5–16. https://doi.org/10.1016/S0926-3373(99)00143-5.

[37] S. Jin, G.H. Dong, J.M. Luo, F.Y. Ma, C.Y. Wang, Improved photocatalytic NO removal activity of SrTiO3 by using SrCO3 as a new co-catalyst, Appl. Catal. B Environ. 227 (2018) 24–34. https://doi.org/10.1016/j.apcatb.2018.01.020.

[38] A. Márquez-Herrera, V.M. Ovando-Medina, B.E. Castillo-Reyes, M. Meléndez-Lira, M. Zapata-Torres, N. Saldaña, A novel synthesis of SrCO3–SrTiO3 nanocomposites with high photocatalytic activity, J. Nanopart. Res. 16 (2014) 1–10. https://doi.org/10.1007/s11051-014-2804-5.

[39] Y. Huang, D.D. Zhu, Q. Zhang, Y.F. Zhang, J.J. Cao, Z.X. Shen, W.K. Ho, S.C. Lee, Synthesis of a Bi2O2CO3/ZnFe2O4 heterojunction with enhanced photocatalytic activity for visible light irradiation-induced NO removal, Appl. Catal. B Environ. 234 (2018) 70–78. https://doi.org/10.1016/j.apcatb.2018.04.039.

[40] T. Degen, M. Sadki, E. Bron, U. König, G. Nénert, The HighScore suite, Powder Diffr. 29 (2014) S13–S18. https://doi.org/10.1017/S0885715614000840.
[41] M.D. O'Donnell, Y. Fredholm, A. de Rouffignac, R.G. Hill, Structural analysis of a series of strontium-substituted apatites, Acta Biomater. 4 (2008) 1455–1464. https://doi.org/10.1016/j.actbio.2008.04.018.
[42] D.N. Wang, Y.Q. Guo, K.M. Liang, K. Tao, Crystal structure of zirconia by Rietveld refinement, Sci. China. Ser. A, Math. Physics, Astron. 42 (1999) 80–86. https://doi.org/10.1007/BF02872053.
[43] F. Dong, A.M. Zheng, Y.J. Sun, M. Fu, B.Q. Jiang, W.K. Ho, S.C. Lee, Z.B. Wu, One-pot template-free synthesis, growth mechanism and enhanced photocatalytic activity of monodisperse (BiO)2CO3 hierarchical hollow microspheres self-assembled with single-crystalline nanosheets, CrystEngComm. 14 (2012) 3534–3544. https://doi.org/10.1039/C2CE06677G.
[44] M. Sosulnikov, Y. Teterin, X-Ray Photoelectron Studies of Calcium, Strontium, and Barium and Their Oxides and Carbonates, J. Electron Spectros. Relat. Phenomena. 59 (1992) 111–126. https://search.proquest.com/docview/25930619.
[45] H. Tan, Z. Zhao, W. Zhu, E.N. Coker, B. Li, M. Zheng, W. Yu, H. Fan, Z. Sun, Oxygen Vacancy Enhanced Photocatalytic Activity of Pervoskite SrTiO3, ACS Appl. Mater. Interfaces. 6 (2014) 19184–19190. https://doi.org/10.1021/am5051907.
[46] S. Ouyang, H. Tong, N. Umezawa, J. Cao, P. Li, Y. Bi, Y. Zhang, J. Ye, Surface-alkalinization-induced enhancement of photocatalytic H 2 evolution over SrTiO 3-based photocatalysts, J. Am. Chem. Soc. 134 (2012) 1974–1977. https://doi.org/10.1021/JA210610H/SUPPL_FILE/JA210610H_SI_001.PDF.
[47] D.S. Shtarev, A. V Shtareva, R. Kevorkyants, A. V Syuy, Synthesis, characterization, optoelectronic and photocatalytic properties of Sr2Bi2O5/SrCO3 and Sr3Bi2O6/SrCO3 heterostructures with varying SrCO3 content, Chemosphere. 267 (2021) 129229. https://doi.org/10.1016/j.chemosphere.2020.129229.
[48] R.A. Shawabkeh, N.M. Faqir, K.M. Rawajfeh, I.A. Hussein, A. Hamza, Adsorption of CO2 on Cu/SiO2 nano-catalyst: Experimental and theoretical study, Appl. Surf. Sci. 586 (2022) 152726. https://doi.org/10.1016/J.APSUSC.2022.152726.
[49] Y.G. Deng, S. Shu, N.J. Fang, R.B. Wang, Y.H. Chu, Z.B. Liu, W.L. Cen, One-pot synthesis of SrTiO3-SrCO3 heterojunction with strong interfacial electronic interaction as a novel photocatalyst for water splitting to generate H2, Chinese Chem. Lett. (2022). https://doi.org/10.1016/j.cclet.2022.03.046.
[50] H. Wang, Y.J. Sun, G.M. Jiang, Y.X. Zhang, H.W. Huang, Z.B. Wu, S.C. Lee, F. Dong, Unraveling the Mechanisms of Visible Light Photocatalytic NO Purification on Earth-Abundant Insulator-Based Core–Shell Heterojunctions, Environ. Sci. Technol. 52 (2018) 1479–1487. https://doi.org/10.1021/acs.est.7b05457.
[51] Z.H. Ai, W.K. Ho, S.C. Lee, L.Z. Zhang, Efficient photocatalytic removal of NO in indoor air with hierarchical bismuth oxybromide nanoplate microspheres under visible light, Environ. Sci. Technol. 43 (2009) 4143–4150. https://doi.org/10.1021/es9004366.
[52] J.-L. Shie, C.-H. Lee, C.-S. Chiou, C.-T. Chang, C.-C. Chang, C.-Y. Chang, Photodegradation kinetics of formaldehyde using light sources of UVA, UVC

and UVLED in the presence of composed silver titanium oxide photocatalyst, J. Hazard. Mater. 155 (2008) 164–172. https://doi.org/10.1016/j.jhazmat.2007.11.043.
[53] Z.P. Yang, Y.B. Shi, H. Li, C.L. Mao, X.B. Wang, X.F. Liu, X. Liu, L.Z. Zhang, Oxygen and Chlorine Dual Vacancies Enable Photocatalytic O2 Dissociation into Monatomic Reactive Oxygen on BiOCl for Refractory Aromatic Pollutant Removal, Environ. Sci. Technol. 56 (2022) 3587–3595. https://doi.org/10.1021/acs.est.1c08532.
[54] X.W. Li, W.D. Zhang, W. Cui, J.Y. Li, Y.J. Sun, G.M. Jiang, H. wei Huang, Y.X. Zhang, F. Dong, Reactant activation and photocatalysis mechanisms on Bi-metal@Bi2GeO5 with oxygen vacancies: A combined experimental and theoretical investigation, Chem. Eng. J. 370 (2019) 1366–1375. https://doi.org/10.1016/j.cej.2019.04.003.
[55] Y.F. Zhang, Y. Huang, S.C. Lee, J.J. Cao, The mechanism of room temperature catalytic C–H dissociation and oxygenation of formaldehyde over nano-zirconia phase-junction, Chem. Eng. J. 380 (2020) 122498. https://doi.org/10.1016/j.cej.2019.122498.
[56] G. Henkelman, A. Arnaldsson, H. Jónsson, A fast and robust algorithm for Bader decomposition of charge density, Comput. Mater. Sci. 36 (2006) 354–360. https://doi.org/10.1016/j.commatsci.2005.04.010.
[57] J.R. Ran, W.W. Guo, H.L. Wang, B.C. Zhu, J.G. Yu, S. Qiao, Metal-Free 2D/2D Phosphorene/g-C3N4 Van der Waals Heterojunction for Highly Enhanced Visible-Light Photocatalytic H2 Production, Adv. Mater. 30 (2018) 1800128. https://doi.org/10.1002/adma.201800128.
[58] Y. Xu, M.A.A. Schoonen, The absolute energy positions of conduction and valence bands of selected semiconducting minerals, Am. Mineral. 85 (2000) 543–556. https://doi.org/10.2138/am-2000-0416.
[59] J. Xiong, J. Di, J.X. Xia, W.S. Zhu, H.M. Li, Surface Defect Engineering in 2D Nanomaterials for Photocatalysis, Adv. Funct. Mater. 28 (2018) 1801983. https://doi.org/10.1002/adfm.201801983.

Credit Author Statement

Shuwen Han: Writing - Original Draft, Data Curation, Investigation. **Xinwei Li:** Writing - Review & Editing. **Yan Tan:** Writing - Review & Editing, Supervision. **Yu Huang:** Project administration. **Zhongbiao Wu:** Project administration. **Meng Wang:** Project administration. **Wingkei Ho:** Writing - Review & Editing. **Shun-cheng Lee:** Supervision, Funding acquisition, Writing - Review & Editing.